AIAA Paper 2004 - 0529
42ND AIAA Aerospace Sciences Meeting & Exhibit
Reno, NV: January 5 – 8, 2004

VALIDATION AND COMPARISON OF WIND AND DPLR RESULTS FOR HYPERSONIC, LAMINAR PROBLEMS

Matthew MacLean* and Michael Holden†
Calspan-University at Buffalo Research Center
Aerothermal / Aero-optics Evaluation Center
Buffalo, NY 14225

ABSTRACT

An examination of the solutions generated using two high-speed computational fluid dynamics codes has been made – the WIND code from the NPARC Alliance, and the DPLR code from NASA Ames Research Center. To evaluate code performance, cases have been selected from the available experimental database compiled by Calspan-UB Research Center (CUBRC). Two basic model geometries have been selected – a hollow cylinder flare, and a $25^O/55^O$ double cone – both of which were studied under conditions to create laminar, axisymmetric flowfields. Solutions were obtained using identical grids for each code to assess the convergence properties and overall performance of the numerical schemes compared both to each other and to the available experimental data.

While the algorithms of the two codes are very different, the solutions obtained for the representative geometries using the perfect gas model were found to be generally consistent. One code was observed to demonstrate some difficulty with very high aspect ratio grid cells. Thus, some care had to be taken to properly construct the grid for it. Despite the high-order formal accuracy of the two codes, both code solution trends were shown to behave as a mixed order scheme over successively refined grids for the problems evaluated.

The effect of vibrational non-equilibrium energy in the freestream was also studied with regard to the consequences of the perfect gas model assumption. The activity of the vibrational energy mode was found to most strongly impact the separation region of the sharp nose double cone case, an effect which was found to offset the error induced by inadequate grid resolution. Further, peak levels of pressure and heating were found to be adequately captured for both the hollow cylinder and double cone models using both the perfect gas and the real gas models.

NOMENCLATURE

C_P	pressure coefficient
C_H	heat transfer coefficient
δ	shock offset distance
E_1	Richardson extrapolation error estimator
f_K	local or global solution quantity on a given grid
G*n*	solution grid number (1=finest, 5=coarsest)
g_i	Taylor series derivative term (constant)
h	grid cell size parameter
i,j,k	structured grid indices
L	characteristic model length
M	Mach number
p	spatial order of convergence
r	ratio of coarse grid to fine grid size (r>1)
R	nose radius
x,y	spatial coordinates

INTRODUCTION

Re-emerging interest in hypersonic flows has created the need for reliable computational tools to predict the complex flow patterns arising from shock interaction on hypervelocity vehicles. One primary example of such an application is the continued interest in SCRAMJET propulsion research. Apart from the internal engine aerothermodynamics itself, this type of engine typically involves an integrated engine/airframe configuration with detailed control surfaces and complex compression inlet ramps. The computational solution of such detailed inlet compression flows to predict the total drag force on the surface, for example, requires a well-validated and well-understood numerical tool.

To facilitate the validation of these types of numerical tools, CUBRC has cultivated a code validation database[1] containing a series of "building-block"-style geometries for which experimental data has been obtained and cataloged using CUBRC's hypervelocity facilities[2]. This code validation database contains a variety of experiments addressing various aspects of hypersonic flow. Typically, each geometric model is tested at several flow conditions to cover a

* *Senior Research Scientist, Member AIAA*
† *AAEC Program Director, Fellow AIAA*

range of flow phenomena. For the data sets pertaining to these model geometries studied here, heat transfer and pressure measurements were made along the length of the wall surface. The pressure coefficient is the comparison standard for pressure given in the database, defined as:

$$C_P = \frac{P - P_\infty}{1/2\,\rho_\infty U_\infty^2} \qquad (1)$$

The heat transfer coefficient is the similar standard for wall heat transfer rate, defined here as:

$$C_H = \frac{q_{WALL}}{1/2\,\rho_\infty U_\infty^3} \qquad (2)$$

EXPERIMENTAL DATASETS

Two distinct types of models have been selected from the code validation database for examination. The first model is called the hollow cylinder flare. This configuration was chosen as a code validation exercise because of leading edge shock / separation shock interactions along the forebody and a complex recirculation zone caused by flow separation that envelopes the compression corner. In the code validation database, data for two different hollow cylinder configurations exist. The first configuration is commonly called the "short flare." It was found, however, that the downstream re-attachment point of the boundary layer can occur right at the back end of the flare (where it connected to the base). Thus, a second configuration was built and tested to avoid this situation. This second configuration is called the "extended flare," as the flare surface extends further downstream to allow a fully reattached boundary layer to develop.

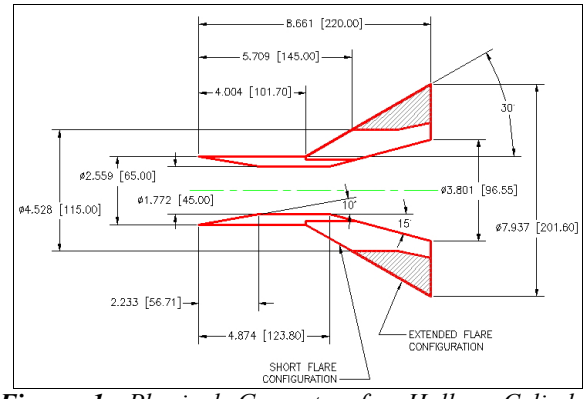

***Figure 1**. Physical Geometry for Hollow Cylinder Model Short and Extended Flare Configurations (all units shown in the format of: inches [millimeters])*

The geometry for both flare configurations is shown in Fig. 1. The extended flare is the only configuration studied in this paper, and, thus, the short flare will not be considered further.

The second experimental case is that of a geometrically axisymmetric biconic, or double cone model. The double cone (and its two dimensional counterpart, the double wedge) has been extensively studied and computationally modeled because of the complex shock interaction structure that results from the compound geometric angle[3]. Such a geometry requires very fine grid resolution to adequately resolve the flow as will be shown in a later section. For the CUBRC code validation database, the double cone was selected to have a 25° and 55° primary and secondary half-angle respectively. Code validation studies for 4 separate nose configurations are available. Here, the sharp nose tip and a nose tip radius of 6.35 mm (0.25") were selected for study. The complete geometry of both double cone configurations is shown in Fig. 2.

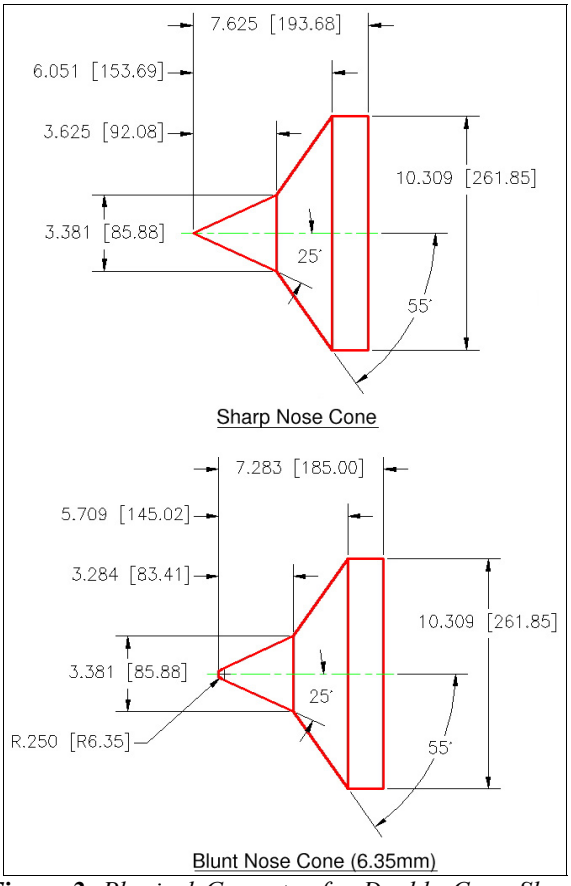

***Figure 2**. Physical Geometry for Double Cone Sharp Nose and 6.35mm Blunt Nose Configurations (all units shown in the format of: inches [millimeters])*

The continued interest the double cone problem is best summarized by Candler, *et al.*[4], where it was noted that grid and physical modeling errors on this type of problem are nonlinearly magnified by viscous-

inviscid interactions. An erroneous enlargement in the separation zone will magnify the interaction strength of the shocks, which then further increases the separation zone – increasing the error beyond the initial level. This feature of the flow geometry creates a truly challenging case from a computational perspective by requiring strict grid quality standards and robust numerical algorithms that can avoid this type of error cycle.

For each geometry, several runs with supporting data are available in the CUBRC database. From these available datasets, one typical run condition has been selected for the hollow cylinder (run 14), one run condition for the sharp nose double cone model (run 35), and one run condition for the blunt nose 6.35 mm double cone model (run 31). The freestream conditions for these three cases are given in Table 1. Freestream data for these and other runs that are available for each geometric model may be found in Holden, *et al.*[5]

The freestream conditions were chosen to be fully laminar to avoid transitional or turbulent effects in the flow. The test gas for all cases is nitrogen, because some of the run conditions in the code validation database are such that significant oxygen dissociation might have occurred with air. Dissociation effects in the freestream and on the model itself have been shown to be insignificant[4], so the fluid has been assumed to be composed of 100% N_2 for all three cases for the purposes of freestream specifications.

Table 1. *Freestream Run Conditions for Selected Code Validation and Comparison Cases*

Freestream Conditions	**Extended Hollow Cylinder Flare**	**Double Cone Study, Sharp Nose**	**Double Cone Study, Blunt Nose**
CUBRC Run	14	35	31
test gas	N_2	N_2	N_2
Mach Number	10.30	12.49	12.43
Velocity, m/s	2,304	2,576	2,621
Pressure, Pa	31.88	18.55	18.27
Temperature, ^{O}K	120.4	102.2	107.0
Vibration Temp., ^{O}K	2,467	2,711	2,772
Density, kg/m^3	8.810E-4	6.081E-4	5.670E-4
Model Wall Temperature, ^{O}K	295.2	295.8	297.0

It is essential to note that non-equilibrium vibrational effects have been shown to be important in obtaining freestream conditions from the nozzle reservoir conditions in shock tunnel facilities that create high enthalpy flows. High temperature and pressure gas in the reservoir created by the shock tube expands through the nozzle so quickly that a significant portion of the energy in the flow can get frozen in the form of vibrational energy, which impacts the resulting freestream conditions for the test. This effect has been extensively studied already by Candler, *et al.*[6] and the information in Table 1 represents the updated results of those efforts by accounting for non-equilibrium effects in the freestream. Initially, the vibrational energy in the freestream (given as a vibrational temperature in Table 1) has been neglected so that a perfect gas diatomic nitrogen model could be implemented in all computational problems for both codes. The effect of the perfect gas model assumption will be assessed in terms of its impact on the wall pressure and heat transfer data.

COMPUTATIONAL TOOLS

Two compressible flow CFD codes have been selected for comparison and evaluation in this study. Both codes are high-order, finite-volume based codes that offer typical options for flux discretization, time integration, variable extrapolation, etc. Solutions for these two codes were compared to experimental data from the CUBRC database as well as compared to each other on identical grids to assess the strengths, weaknesses and general capabilities of each code.

The WIND code from the NPARC alliance[7] is a general purpose compressible code with a rich array of features. Several flux splitting and flux difference splitting discretization schemes are available covering most of the commonly implemented methods – Roe, Van Leer, and other commonly known schemes. The WIND code default convective scheme is a second order Roe operator. Variable extrapolation is handled by a MUSCL-type TVD method employing the MIN-MOD limiter by default. For viscous solutions, this code solves the full Navier-Stokes equation set. WIND offers finite-rate or frozen chemistry options, as well as a wide range of turbulence models, although the issues of turbulence and chemical modeling will not be dealt with in depth in this paper.

The DPLR code from NASA Ames Research Center is a hypersonic code based on the data parallel line relaxation (DPLR) method[8]. The DPLR method has been designed for efficient parallel processing through an implicit coupling mechanism. The algorithm works by tightly coupling the body normal direction gradients into the implicit operator as these gradients will physically dominate the flow. By relaxing gradients in the other directions to a known solution level, a series of sweeps on each body normal "line"

allows for an algorithm that may be set up to be very efficient in parallel. The secondary advantage is that the nature of the coupling in the algorithm allows steady state problems to be run at very high CFL numbers once the initial, short-wave, transient errors have been damped out. The DPLR code uses a modified Steger-Warming flux splitting algorithm to discretized the convective term along with third-order MUSCL extrapolation using the MIN-MOD limiter. The modification to the flux splitting algorithm reduces the artificial dissipation found in the original Steger-Warming method. The DPLR code also provides a detailed library of chemical models and capabilities. Thus, DPLR is a capable general purpose compressible code, but is most effectively used for hypervelocity, viscous flow problems.

Both codes require structured grids to define the computational domain, and both can solve 2D planar, 2D axisymmetric, and 3D problems. Both WIND and DPLR are set up to run in parallel on large multi-processor machines or clusters.

VALIDATION AND VERIFICATION

The issue of modeling uncertainties is a central part of any CFD computation, particularly in computations involving complex, hypersonic flows. From Blottner[9], the concept of validation may be described as "solving the right equations," while verification may be described as "solving the equations right." This simple description separates possible code modeling errors into two basic categories.

Validation is the issue of physical modeling errors. Here, the goal is to assess the capability of the numerical schemes implemented in these two high speed codes to correctly predict the complex physics of the physical model by comparing to the established experimental data. Verification, in contrast, is the issue of numerical errors like boundary condition placement, incomplete convergence to steady state, numerical round-off error, and – in particular – grid dependency, or ordered discretization error. For example, a solution generated on a very coarse or poorly constructed grid using one of these codes may compare very poorly with the experiment, but this says more about the grid than it does about the numerical method or the code itself.

These issues will be discussed in looking at the results to be presented, and they will be addressed in general conformance to the established guidelines set forth by the AIAA[10]. Since grid dependence error is typically the major contributor to verification issues in CFD, particular attention will be paid to it.

For structured grids, the most common method of computing grid dependence error is using Richardson extrapolation[11]. The essence of this method is to generate a solution to the problem on several successively (uniformly) refined grids and compare the solution of a representative quantity on those grids.

The matrix of computational model sizes for all problems of interest is given in Table 2. Listed are the grid sequences for each case type, where a grid sequence is formed by taking the finest grid and keeping only every N^{TH} grid point in both directions. Sequenced grids are numbered from 1 (finest) to 5 (coarsest), and are listed by the number of cells (not points).

Table 2. *Computational Test Matrix with Number of Grid Cells for each Physical Case*

CFD Case		***Sharp Nose Double Cone***	***Blunt Nose Double Cone***	***Hollow Cylinder Ext. Flare***
WIND & DPLR Grid Sequences (I x J Cell Size)	G1	2048 x 768	2048 x 768	N/A
	G2	1024 x 384	1024 x 384	1000 x 320
	G3	512 x 192	512 x 192	500 x 160
	G4	256 x 96	256 x 96	250 x 80
	G5	128 x 48	128 x 48	125 x 40

One may see that there is no G1 grid for the hollow cylinder case. The double cone computations were found to require more grid points to sufficiently resolve the flowfield, and the grid sequences were numbered such that a given G# corresponds roughly to the same total number of grid cells for all case types. Thus, the G2 grid is roughly the same size for both the hollow cylinder and the double cone. While grid sizes of the form 2^N cells are common, the WIND code allows a maximum of 1,023 points in a single block without inter-zonal breaking. Thus, a G2 grid with a size of slightly less than this value was preferred here for the hollow cylinder flare to allow WIND to solve the G2 grid as a single numerical block without the additional complexity of inter-zonal boundaries. The double cone cases were solved using parallel processing, so this limitation was not a consideration.

A Taylor series expansion may be written for the known discrete solution on each finite grid in terms of the exact solution for an infinitely dense grid and the discrete grid size, h. This expression may be written for any single degree of freedom or for a globally calculated quantity like lift or drag. Details of the derivation may be found from Roache[11]. A researcher may use the generated solutions on m discrete grid levels to eliminate at least the first m derivative terms of the final expression, creating an error measure accurate to $O(h^{m+1})$. If the computational method is known to be greater than first order in space, then one or more derivative terms are known to be zero and the accuracy

of the collective expression can be made greater than $O(h^{m+1})$. In summary, knowing a solution on two grids, for example, (where grid 1 is the finest grid and grid 2 is a coarse grid) allows the calculation of the Richardson extrapolation error estimator, E_1, given by Eqn. (3) for any computational method of known order of convergence, p.

$$E_1 = \frac{f_2 - f_1}{f_1\left(r_{12}^P - 1\right)} \qquad (3)$$

This error estimator may be shown to be equivalent to the percent difference between the exact solution and the finest grid level solution, f_1, accurate to $O(h^{p+1})$. Note that this is a signed error estimator. The solution on the fine grid may be therefore represented as shown in Eqn. (4).

$$f_{EXACT} = f_1 * \left(1 - E_1\right) + O\left(h^{p+1}, E_1^2\right) \qquad (4)$$

Although it is possible to use Eqn. (4) to actually correct the fine grid solution, this practice is not recommended as it can have secondary effects on solution quality[12]. Instead, these authors prefer to treat the fine grid solution as the best available solution and use Eqn. (4) as a known discrete error estimation for this solution.

Finally, if more than two discrete solutions are known, it is possible to further increase the accuracy of the error estimator, E_1, or calculate the observed order of accuracy, p, of the code for the particular problem in question. This is a useful opportunity as the observed order of the solution may be quite different than the formal order of the code. Factors such as boundary treatment, convergence or round-off issues, and the presence of shocks can all lower the observed order of accuracy of a method below its formal order. As the recent work of Roy[12] shows, multiple studies have confirmed that higher-order solutions of flows containing shocks will revert to first order as cell size approaches zero even if flux limiting is removed. Roy surmises this effect to be caused by the rate of information transmission through the shock. Thus, it is important to find the observed order of convergence rather than making a general assumption about it.

HOLLOW CYLINDER RESULTS

The hollow cylinder extended flare problem corresponding to CUBRC Run 14 was solved numerically with both WIND and DPLR. Freestream specifications were input to the codes from Table 1 in the proper units for each code (English for WIND, SI for DPLR). Shown in Fig. 3 is the G5 grid for this computational case. Note again that this same grid (scaled for unit consistency) was used for each code, eliminating the issue of grid differences between the two solutions. The G5 grid is just the same as 1 out of every 8 grid lines in each direction of the finest level for the hollow cylinder, the G2 grid. This coarse grid is shown purely for clarity in the picture. A small block of inlet cells was placed at the leading edge of the cylinder to facilitate application of the boundary conditions.

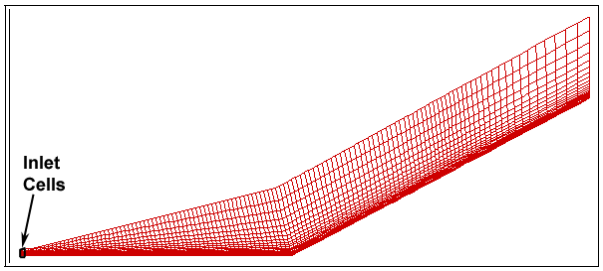

***Figure 3**. Hollow Cylinder Extended Flare G5 Grid Computational Model, 125 x 40 (1/8TH Finest Grid Density Shown)*

The problem is axisymmetric and all solutions for this case were performed using a single numerical block on a Pentium-4 Linux workstation with 1GB of available physical memory.

The flow field solution is shown in Figs. 4 and 5, which show the Mach number and static temperature of the field respectively. The major shock patterns are clearly visible in the flowfield. Although the WIND solution has been shown, it should be noted that the DPLR solution was visually identical on the finest grid level. Thus, it has not been shown to avoid redundancy.

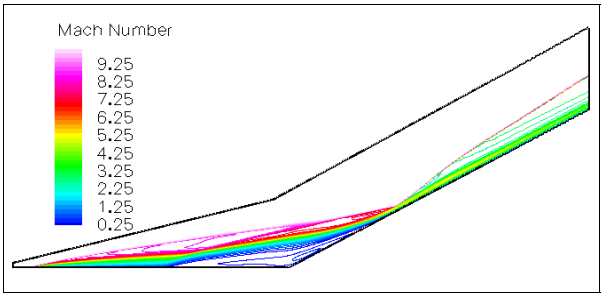

***Figure 4**. Mach Number Contours of Hollow Cylinder Extended Flare Run 14 Solution on G2 Grid(1000 x 320)*

Visible in Fig. 4 is the shock resulting from the leading edge boundary layer bluntness. Approximately half way down the cylindrical section, boundary layer separation may be seen resulting from the shock induced pressure gradient. The separation length is visible, with the flow reattaching itself just over one-third of the distance up the flare section. Looking back at Fig. 1, one may see that this re-attachment location is indeed close to the end of the short flare configuration, which is why the extended configuration was conceived

and tested.

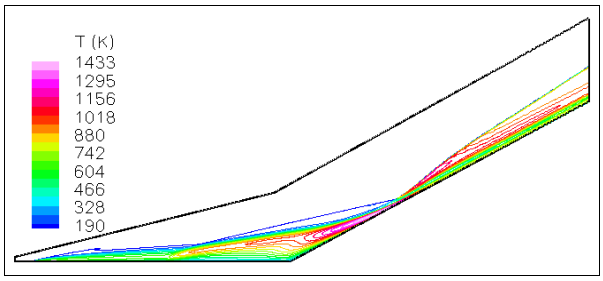

***Figure 5**. Temperature Contours of Hollow Cylinder Extended Flare Run 14 Solution on G2 Grid (1000 x 320)*

The WIND and DPLR solutions may more effectively be contrasted by comparing the results of the surface data with the experimental measurements. Figure 6 shows both the WIND and DPLR solutions for the G2 grid. Both pressure and heat transfer characteristics are given in coefficient form as already described by Eqns. (1) and (2).

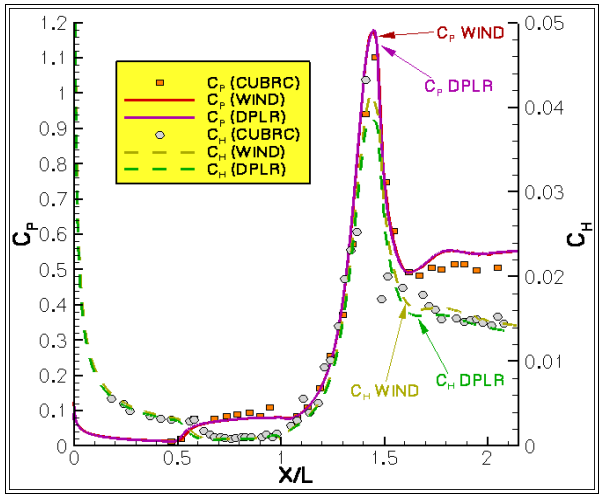

***Figure 6**. Comparison of WIND and DPLR Solutions to Experimental Data for Run 14 Hollow Cylinder Extended Flare Model, G2 Grid (1000 x 320)*

One can see immediately for this case that both codes follow the experimental data trends to a reasonable degree of accuracy. As Fig. 6 shows, the pressure traces along the wall are identical for both codes. The separation zone is well-captured in both cases, and the solutions for the peak pressure along the inclined surface agree well with both the experimental peak value and each other.

In the case of heat transfer, there is some slight under-prediction of maximum heating rate by both codes, but this appears to be a function of grid density in the region of the peak (which is very narrow). There are also some insignificant differences apparent between the two numerical traces, although both codes do a reasonable job of capturing the experimental data points. As heat transfer rate involves evaluation of a derivative and extrapolation from the cell center to the wall, calculation of this quantity can be challenging to compute accurately. Both codes output heat transfer rates and coefficients directly from their post-processing modules, so any small variations between the two could have as much to do with the individual post-processing algorithm as the solution numerics.

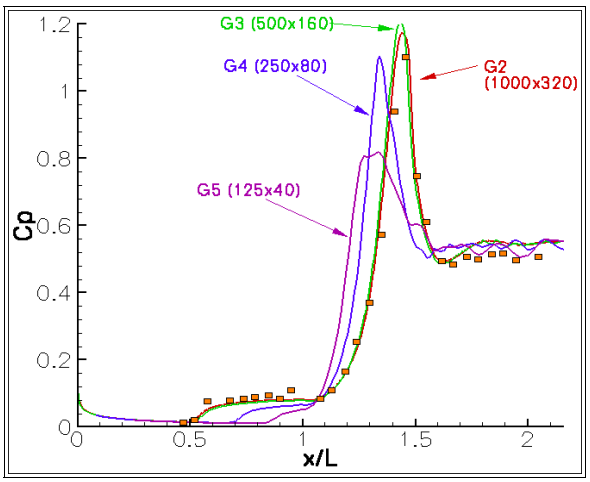

(a) WIND

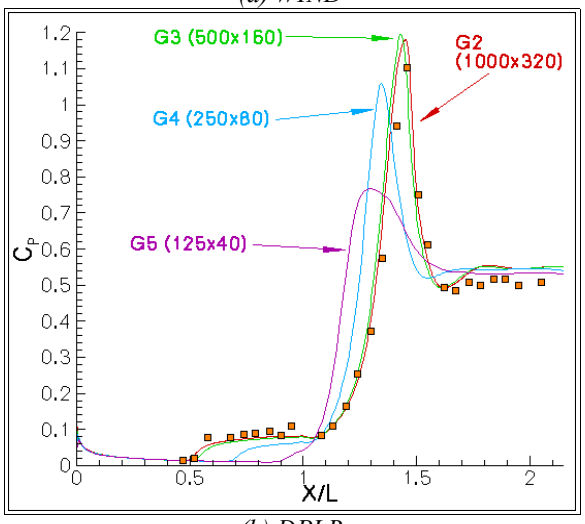

(b) DPLR

***Figure 7**. Pressure Coefficient, C_P, Along the Surface of Hollow Cylinder Run 14 for WIND (a) and DPLR (b) Shown for All Grid Levels, G2 - G5*

One may look at the the grid convergence characteristics of the two codes by looking at the solutions over several successive grids, G2 through G5. In Fig. 7, the solution for pressure coefficient, C_P, for the WIND and DPLR codes is shown corresponding to the sequenced grids. One may see in both cases that good grid convergence is obtained on the G2 and G3 grid levels. The two coarsest grids are clearly not adequate, as both separation size and peak pressure

levels are under predicted. It is also worthwhile to note that the solution on each given grid is virtually identical between the two codes, indicating that their observed order of convergence is similar.

The validity of the perfect gas model was also assessed for this case. The DPLR code contains modeling for both finite rate chemistry and vibrational non-equilibrium, so a case was run using this code on the G2 grid with both options active. The chemistry modeling for this case was a 2-species nitrogen model (N_2 and N) with a single finite-rate reaction. Freestream conditions for the extra degrees of freedom have been evaluated in previous studies[6]. The vibrational temperature of the freestream is given in Table 1 and the freestream gas composition boundary condition is 100% N_2.

Figure 8 shows the ratio of the vibrational to the total energy from this DPLR solution. One can see that even for nitrogen, the flow does get a significant portion of its total energy from vibration due to the elevated vibrational temperature in the freestream.

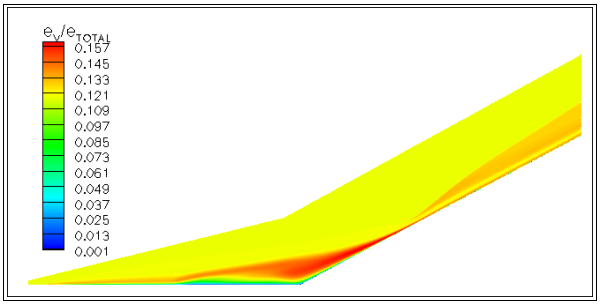

***Figure 8**. Ratio of Vibrational to Total Energy in Flow Field for DPLR Vibrational Non-equilibrium Model on G2 Grid*

Once passing through the leading edge bluntness shock, however, the density is increased sufficiently such that the levels begin to equilibrate. Upon reaching the wall, the vibrational non-equilibrium model makes only a small impact on the solution when compared to the experimental data and the corresponding perfect gas solution, as shown in Fig. 9. Although not shown, dissociation effects within the flowfield were found to be negligible as the flow retained a nominally 100% N_2 composition throughout the domain.

In summary, one finds that by using a perfect gas model, both codes can do an adequate job of predicting the solution of the hollow cylinder extended flare for run 14 from the CUBRC database on a sufficiently fine grid. One also sees that the effect of vibrational temperature on this particular solution is small in terms of the desired solution quantities. Between the perfect gas and vibrational non-equilibrium models, Fig. 9 shows that the peak pressure coefficient changes by only 3% while the peak heat transfer rate at the re-attachment point changes by only 5.5%. The separation point on the forebody is nominally unaffected by the addition of vibrational energy.

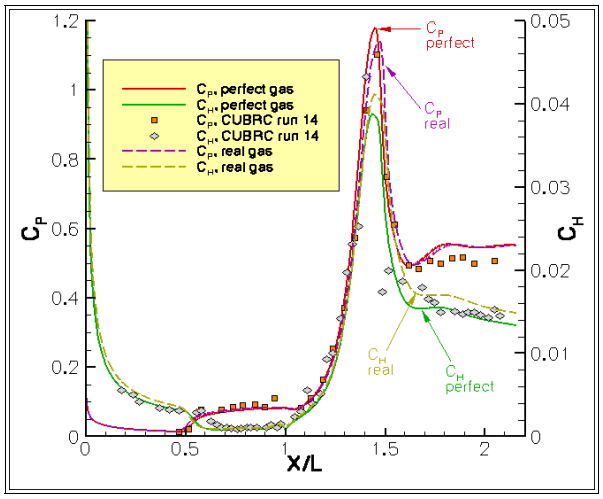

***Figure 9**. Comparison of Wall Data for Perfect Gas and Non-equilibrium Models with DPLR Code on G2 Grid*

SHARP NOSE DOUBLE CONE RESULTS

The complexity of the double cone problem is greater than the hollow cylinder case discussed previously because of the additional shock interaction effects that occur as a result of the compound angles. Figure 10 shows a schematic of the type of flow interaction pattern expected to result from this type of geometry under the conditions studied in these cases. This geometry produces a large separation region spanning the corner between the cones. A shock caused by flow separation interacts with the leading edge oblique shock caused by effective bluntness from the boundary layer. Farther up on the second cone surface, a shock interaction occurs near the reattachment point, causing a strong bow shock with a resulting subsonic region of flow and a supersonic jet close to the surface.

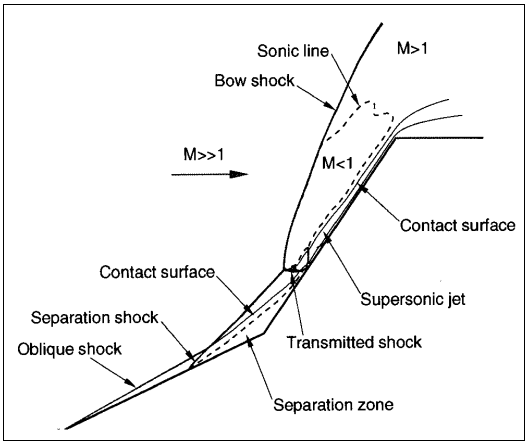

***Figure 10**. Schematic of Double Cone Flowfield (from Ref 14)*

In similar fashion to the hollow cylinder flare case, the sharp nose double cone model was analyzed using both WIND and DPLR over several successive grids, defined in Table 2. For the sharp nose cone, conditions corresponding to run 35 from the CUBRC database were used. The G5 grid for this case is shown in Fig. 11, representing 1 out of every 16 grid lines on the finest grid level. This coarse grid is shown for clarity.

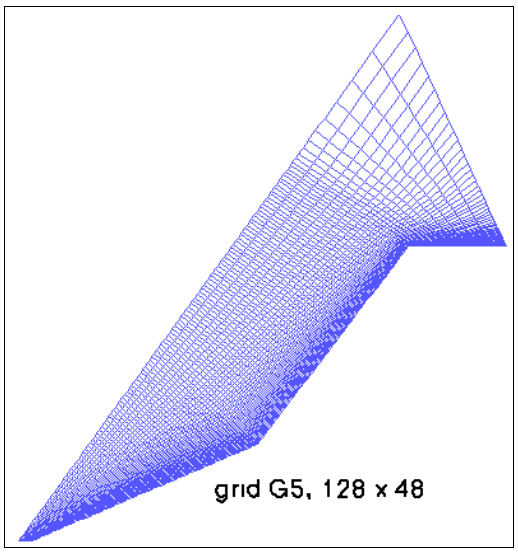

***Figure 11**. Double Cone Sharp Nose Computational Model, G5 Grid, 128 x 48 (1/16TH Finest Grid Density Shown)*

Several different grids were used in the initial investigation of this case with different relative spacing and wall-normal spacing. At first, a grid was created with very tight wall-normal spacing along the entire surface, both in the attached and separated regions of the domain. After exhaustive investigation of that grid and its sequences was completed with both codes, the WIND code displayed significant convergence issues caused by shock instability through the separated region. This is presumed to be a manifestation of the error magnification issue already discussed by Candler, *et al.*[4], who noted that an error in the shock/separation interaction structure tend to magnify other numerical errors in the flowfield as solution proceeds rather than the normal damping of unsteady features as seen in many problems. The DPLR algorithm however, showed none of this unsteadiness. This is to be expected since it is a hypersonic code designed to work with very high aspect ration grids.

With that initial grid sequence, the WIND code did not converge to a steady-state solution, even after running it for a large number of cycles. Although the general flowfield trends resembled the correct solution on the basis of qualitative, visual inspection, the heat transfer and pressure coefficients along the wall surface were tracked as the solution proceeded. After a large number of cycles, the solution structure could be seen to oscillate slowly back and forth repetitively. Levels for both pressure and heat transfer near the reattachment point were typically predicted to be too high by a factor of nearly 2.0. This trend continued apparently indefinitely, as one of the high aspect ratio grid sequences in WIND was run for more than 300,000 cycles with no steady-state convergence found. Other sequences of that same grid displayed similar behavior with the WIND code. The DPLR code did not display this behavior, and demonstrated smooth steady-state convergence behavior at all grid sequences.

Figure 12 shows the surface pressure and heat transfer levels from the DPLR code for this grid at the densest level, along with experimental data from CUBRC database run 35 for comparison. Also shown is the result from the un-converged WIND model after more than 300,000 cycles. This demonstrates the type of behavior seen from the WIND code for this particular grid. The peak pressure coefficient level for this solution is 5.51 while the peak heat transfer coefficient was predicted to be 0.330. These peak values are clearly not correct, nor are the separation and re-attachment point locations.

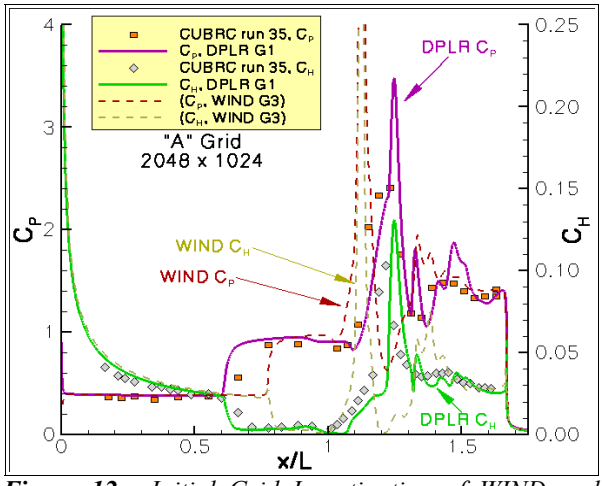

***Figure 12**. Initial Grid Investigation of WIND and DPLR Solutions for Run 35 Sharp Nose Double Cone*

After some investigation, several pieces of information were discovered with regard to this situation. It was discovered that the main problem in obtaining convergence with the WIND code was caused by wall-normal spacing in the separated region. As Fig. 12 shows, WIND computes the solution correctly up to the point of separation with this similar wall-normal spacing. This shock oscillation behavior was found to be the same in WIND using the default Roe/physical scheme, the HLLE scheme, and the Van Leer scheme, thus demonstrating that artificial dissipation from the convective scheme is not causing the problem. It is unclear whether this effect seen with the WIND code is

a result purely of the wall spacing, or whether this effect is a result of the time step taken as a result of the wall-normal spacing. Previous researchers have found with this geometry that a large enough CFL value can prevent steady-state convergence. However, tests of WIND with CFL values ranging from 0.1 to 1.5 to converge the separation region failed to produce any steady results.

After working with this issue for some time and testing several different variations of the grid, the final grid sequence was created. The main difference between the final grid and the original grid is that the wall normal spacing was made coarser in the separated region. For the final grid sequence (shown in Fig. 11), wall normal spacing was kept on the order of 2μm (0.0001 in), which is between one and two orders of magnitude larger than the original grid.

The solutions on this final grid yielded much improved solution quality and convergence performance from the WIND code for most grid levels. Even with this final grid, however, the finest level, G1, began to show some of the same behavior as did the original solutions from Fig. 12. However, grid sequences G2 through G5 performed well with the WIND code, as shown in Fig. 13. This figure therefore shows the G2 grid solution for the surface heat transfer and pressure coefficient. Here, the WIND solution matches the trends in the surface data for both pressure and heat transfer closely. While the peaks for both heat transfer and pressure coefficients show somewhat higher values than the maximum data point in each case, this is to be expected since the resolution in the numerical code is much finer than the experimental gages. Both the separation point and the peak/re-attachment area show close corroboration with the data.

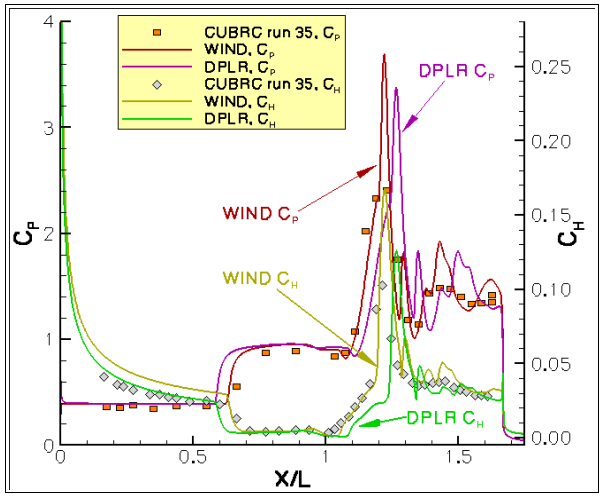

***Figure 13**. Grid Comparison of WIND and DPLR Solutions for Run 35 Sharp Nose Double Cone, G2 Grid (1024x384)*

By comparing the surface solutions that may be considered "good" as given in Fig. 13 from both codes, it may be seen that – given the perfect gas assumption – the WIND code seems to predict the separation and reattachment point somewhat better than DPLR, although the peak levels and trends are generally captured with both codes. Previous work by Candler, *et al.*[14] found that the choice of convective numerical scheme made a large impact on the converged solution to the double cone problem. They studied the effect of numerical scheme, limiter, and formal order, finding that all three could change the solution obtained. Here, WIND uses by default a Roe-type scheme, while DPLR uses a modified Steger-Warming scheme. Although the newer, modified Steger-Warming scheme drastically reduces dissipation found from the original version, a Roe scheme will still provide smaller artificial dissipation levels. Although no time was available to explore the solutions provided by the WIND code for anything other than the default Roe scheme, a point of interest for future study would be to see if the Van Leer convective scheme in WIND (which is known to have very high dissipation levels) produces a solution which is different than the Roe scheme does on a similar grid.

In looking at the DPLR solution, one sees reasonable overall agreement with the trends of the experimental data. Pre-separation levels show a reasonable if slightly conservative prediction. Pressure up to the point of separation is approximately constant on the front cone as it should be. When considering one of the most important aspects of the problem is to predict the peak levels of pressure and heating against the surface, the DPLR code perform this function adequately in that it predicts these values conservatively. Also, the separation length is captured, although slightly over-predicted. This issue will be addressed later. Further, by comparing Fig. 13 with the previously given Fig. 12, one may see that the solution from the DPLR code is unchanged to any significant degree. This shows that DPLR, at least, is providing truly grid independent solutions given sufficient resolution despite a significant change in the grid structure and spacing in a critical region.

The solution of the flowfield for the sharp nose double cone for run 35 may be best shown by looking at the computational Schlieren image of the flowfield, which was created as a grayscale image of the magnitude of the density gradient. This result is shown in Fig. 14. It shows the solution on the G2 grid from the DPLR code, which was used over the G1 grid to minimize post-processing time. Grid independence is achieved between the G1 and G2 grid sequences, so the solutions on these two grids are interchangeable for flow visualization purposes. Also, it is important to note that, for visualization purposes the WIND and DPLR solutions on the G2 grid look very similar, so the choice of one particular code solution over another is arbitrary.

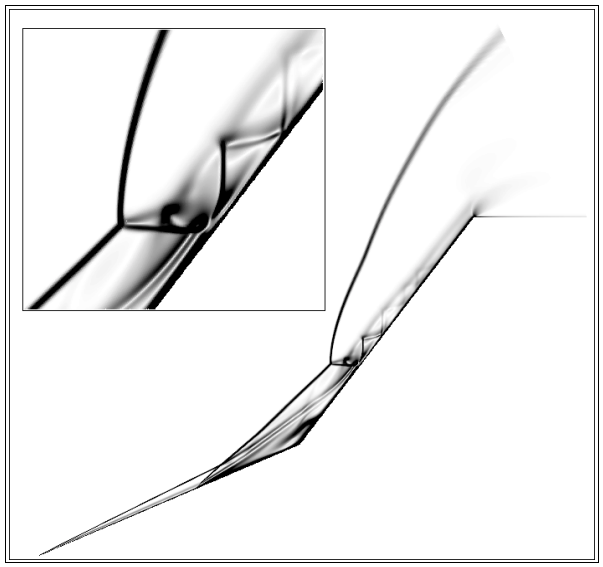

***Figure 14**. Density Gradient Solution from DPLR Code, G2 Grid, 1024 x 512 for Sharp Nose Run 35 with Enhancement of Shock Interaction Region*

All the major shock features are clearly shown exactly as they were illustrated in the schematic in Fig. 10. As with Schlieren photography, where higher density gradient values cause increased optical shift in the light waves, the stronger shocks are darker than weak ones. For example, the bow shock is very dark near the reattachment point in front of the subsonic region, but it gets increasingly lighter as the inclination decreases and it becomes more oblique. The resolution in the shock interaction region is also evident, as the trailing contact surface and oblique shock reflection in the supersonic jet are clearly defined. The contact surface surface bordering the top of the separation zone is also visible on the full image, and can be seen on the shock interaction enhancement where the flow re-attaches below the transmitted shock.

Further, the Mach number gradients from the DPLR solution on the G2 grid is show in Fig. 15. Here, the subsonic region has been highlighted by removing all contour coloring below 1.0. Thus, the sonic line specified from Fig. 10 is clearly outlined and some measure of the separation region is also shown since the velocity is relatively low in that region.

To demonstrate that the solutions do indeed look similar, the WIND solution from this same grid is shown in Fig. 16. Qualitative examination of the two solutions show no significant differences, as the subtle shifts in separation length between the two codes that was shown in Fig. 13 are not apparent from a visual inspection.

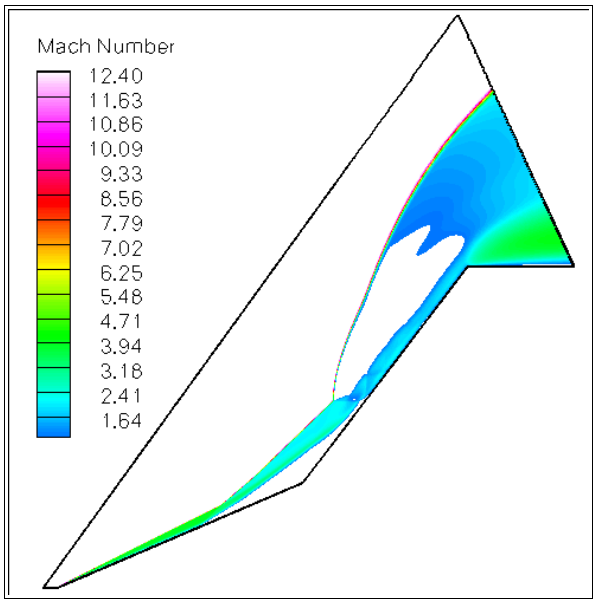

***Figure 15**. Supersonic Mach Number Solution for Sharp Nose Run 35, G2 Grid, 1024 x 384, from DPLR Solution*

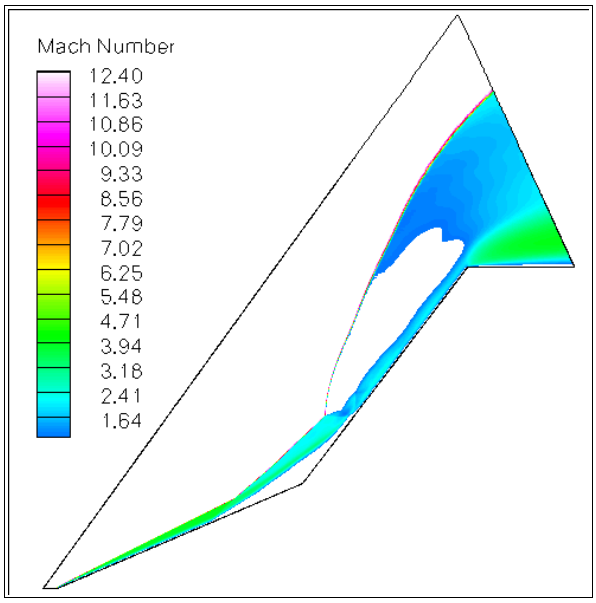

***Figure 16**. Supersonic Mach Number Solution for Sharp Nose Run 35, G2 Grid, 1024 x 384, from WIND Solution*

Grid independence is demonstrated for this case using the wall pressure coefficient data from the successively sequenced grid, G1 through G5. The solutions are shown in Fig. 17. For WIND, the G1 grid has been excluded based on a previous discussion. That solution is shown as a dotted line in Fig. 17(a) simply for reference and to demonstrate the effect that was seen with dense grid resolution. Here, grid independence is again achieved at the finest grid levels. Compared to the hollow cylinder, a higher grid density was required

to remove large ordered discretization error effects from the solution.

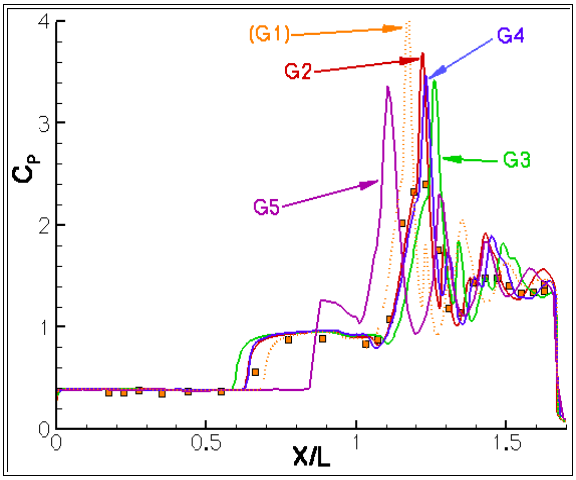

(a) WIND

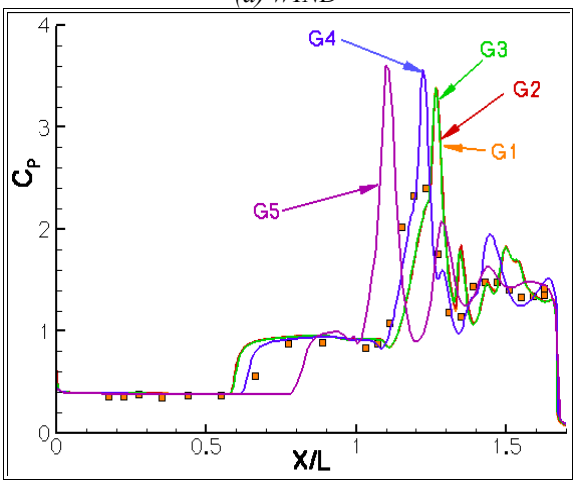

(b) DPLR

***Figure 17**. Pressure Coefficient, C_P, Along the Surface of Sharp Nose Double Cone Run 35 for WIND (a) and DPLR (b) Shown for All Grid Levels, G1 - G5*

Finally, the effects of the assumption of perfect gas with no vibrational energy will be assessed. As with the hollow cylinder flare case, the DPLR code was used with finite rate chemistry and finite rate vibrational relaxation using the freestream vibrational temperature given in Table 1. The result of this comparison for the G2 grid is given in Fig 18. Here, the effects of vibrational non-equilibrium are somewhat more pronounced than in the case of the hollow cylinder flow. Generally, however, one may see that the overall trends are the same for both the perfect gas and the real gas models. Also, both gas models predict a consistent level of peak heating and pressure.

The most noticeable difference is that the perfect gas case predicts a larger separation zone than the real gas case does. The separation region is shown in an enlarged view on Fig. 18 to illustrate this feature, which demonstrates the separation point moving downstream by an *x/L* of approximately 0.05 in the case of the real gas model . Nompelis, *et al.*[14] found a similar effect for CUBRC run 28, where they showed this same trend to be more pronounced than in run 35 (studied here). They also found similarly for that case that the separation zone was over-predicted on sufficiently fine grids if one does not also account for non-equilibrium vibrational effects. Here this effect is less prominent than in run 28, but still present. The issue of interest is that insufficient grid resolution and perfect gas modeling create errors that tend to cancel each other out, producing a result that looks deceptively correct.

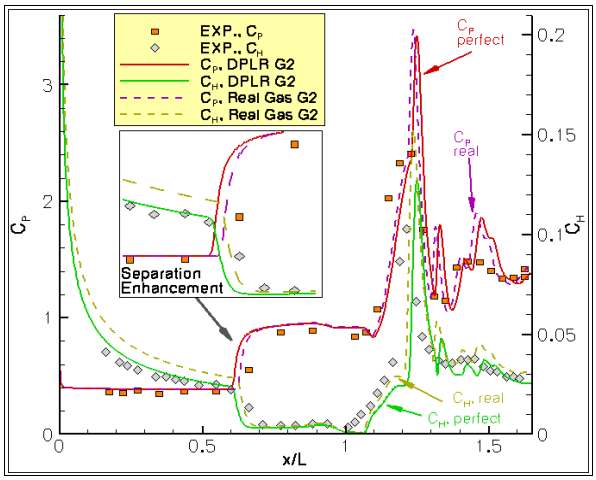

***Figure 18**. Comparison of Sharp Nose Wall Data Results for Perfect Gas and Real Gas Models using G2 Grid with DPLR Code*

Although perhaps not as critical, the heat transfer rate on the front of the forward cone ahead of the separation point also shows some dependency on vibrational effects. This part of the surface was shown to have slip wall effects as a result of the no slip boundary breakdown as discussed by Nompelis, *et al.* for run 28, and a similar issue seems to be present for this case. Although the perfect gas model appears to be predicting leading edge heat transfer rates better than the non-equilibrium model, the slip effect needs to be accounted for to correctly match the experimental heat transfer rates. The effect of slip wall boundary conditions was not studied here at all, except to note that once again the perfect gas model can result in two erroneous features which tend to cancel out and produce a seemingly correct solution.

One interesting area for future exploration may be seen by comparing Fig. 18 with Fig. 13. As the solution with the WIND code demonstrates, the choice of numerical scheme can make a big impact on the solution. It is not clear from the results obtained so far, what effect having a low-dissipation scheme like the Roe scheme might have when coupled with vibrational

non-equilibrium effects. A change in the separation size caused by the inclusion of vibrational non-equilibrium in the WIND solution, for example, would shift the separation zone farther from the observed experiment, indicating that there might be other secondary effects which may be creating further error cancellation in the perfect gas solution.

BLUNT NOSE DOUBLE CONE RESULTS

As with the sharp nose problem, the solutions with the WIND code were found to oscillate indefinitely with no steady-state convergence if the wall-normal cell spacing was made too restrictive. Here too, an investigation was made with several different types of grids with different wall-normal cell spacings. Readers are referred to the previous section on the sharp nose double cone results for a more detailed discussion of that problem. The G5 grid for the blunt nose double cone with a 6.35 mm (0.25") radius nose is shown in Fig. 19. The grid cell arrangement was kept as consistent as possible with the sharp nose grid shown in Fig. 11, with the obvious alteration in the nose region. Wall normal spacing was preserved between the sharp and blunt grids. Again, the G5 grid is 1 out of every 16 grid lines on the G1 grid.

The overall flowfield behavior for blunt nose run 31 was expected to be similar to the sharp nose case of run 35. Similar freestream conditions were used between the two cases as outlined in Table 1 with the exception of the geometric radius of the nose of the front cone. Therefore, the general goal will be to assess whether there is any bluntness effect caused by the nose radius and whether the addition of a nose radius impacts the separation region length in any way.

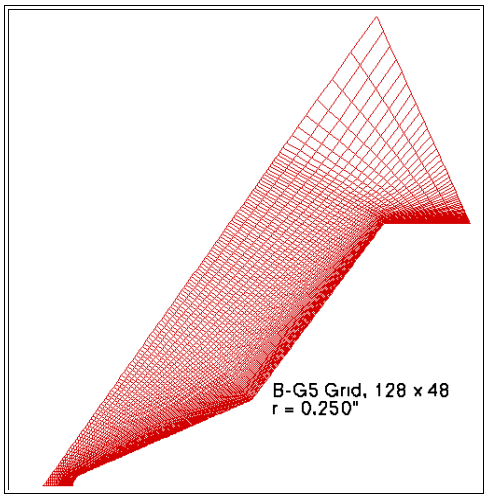

***Figure 19**. Double Cone Blunt Nose Computational Model, G5 Grid, 128 x 48 (1/16TH Finest Grid Shown)*

The density gradient solution on the G2 grid is shown in Fig. 20 just as it was for the sharp nose grid. One can see from the interaction region view that this part of the flowfield is similar to that shown for the sharp nose case in Fig. 14. While the bulk of the flowfield is similar to the sharp case, there is a difference in the shock pattern in the region of the nose tip. Figure 20 also shows a view of only that nose region. The resolution of the flow field allows for a measure of shock stand-off distance at the nose tip and shows the reduction in shock strength as the nose bow shock transitions from normal to oblique. The offset at the nose may be estimated from simple expressions for shock stand-off distance at hypersonic speeds for various geometries. For a blunt cone, this formula is given as[15]:

$$\frac{\delta}{R} = 0.143\, e^{3.24/M_\infty^2} \qquad (5)$$

This estimate predicts 0.927 mm based on the freestream Mach number of 12.43 from Table 1. The scale shown in Fig. 20 gives the distance in meters of about 0.9 mm, showing good agreement with the simple correlation. This sort of agreement lends general credibility to the calculations performed.

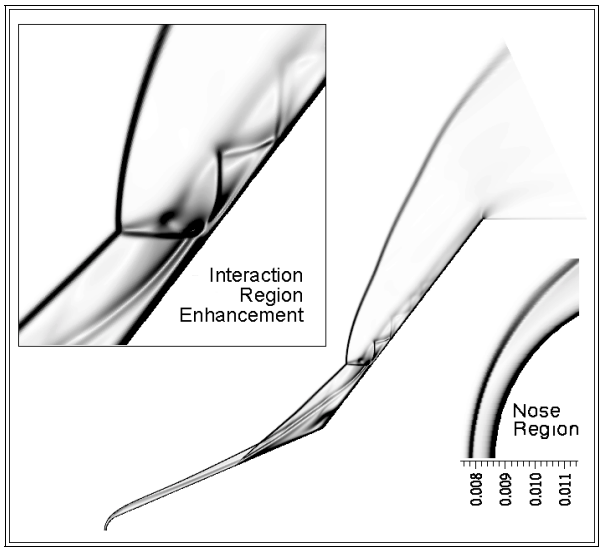

***Figure 20**. Density Gradient Solution from DPLR Code, G2 Grid for Blunt Nose Run 31 with Enhancement of Shock Interaction Region*

Next, the Mach number solution for this case is given. Figure 21 shows this flowfield quantity. In the full model view, the subsonic portion of the flowfield has been eliminated to highlight the subsonic region downstream of the shock interaction region that is caused by the strong bow shock. This part of the field looks similar to the sharp nose case seen in Fig. 15. The separation region length is also similar to the previous case, separating at approximately *x/L* of 0.7 and re-attaching at approximately *x/L* of 1.25. Also

shown is a close view of the nose region. In this view, lines of constant Mach number are drawn, with the sonic line annotated. Line coloring is consistent with the coloring of the full view. This view of the nose also shows the initial stage of boundary layer development along the wall of the curved surface.

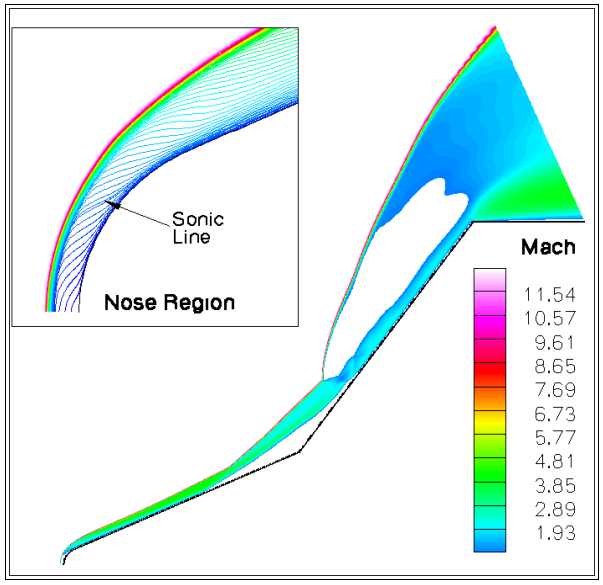

Figure 21. *Mach Number Solution for Blunt Nose Run 31, G2 Grid, 1024 x 384, from DPLR Solution with Nose Region Enhancement*

The result of comparison of the surface data with the experimental finding for CUBRC database run 31 is shown in Fig. 22. Here again, the G1 grid was found to be too dense at the wall and failed to produce a steady solution in WIND; thus, the G2 grid has been used for comparison.

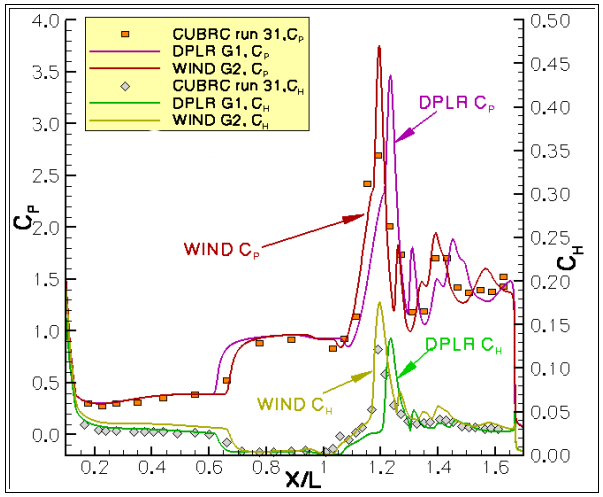

Figure 22. *Comparison of WIND and DPLR Solutions for Run 31 Blunt Nose Double Cone, G2 Grid (1024 x 384)*

Overall, the consistency between the two codes is similar as it was for the sharp nose case, run 35. Here, the separation enlargement resulting from the Steger-Warming dissipation in the DPLR code is slightly less apparent, but still predicts a somewhat larger separation region than the WIND code with the Roe scheme. In this case, however, one can also see the effect of leading edge bluntness on the pressure solution near the front of the model. In the case of the sharp nose data shown in Fig. 14, the pressure coefficient was constant up to the point of flow separation. Here, there is a significant variation caused by the nose radius – a feature that is correctly represented by both codes.

Similar to the sharp nose case, surface pressure coefficient trends were used to assess grid dependency error over the sequenced grids, G1 through G5. The trends are not reproduced graphically here since they look similar to the sharp nose case shown in Fig. 17. Like that case, only at the finest grid levels does the separation point and the peak level and position remain constant, indicating that on the order of 1 million grid points are required to adequately resolve this type of flowfield. The significant feature difference here in the blunt nose model – the nose bluntness effect – is captured equally well on all grid levels in both codes. Thus, even a coarse grid will capture this particular effect.

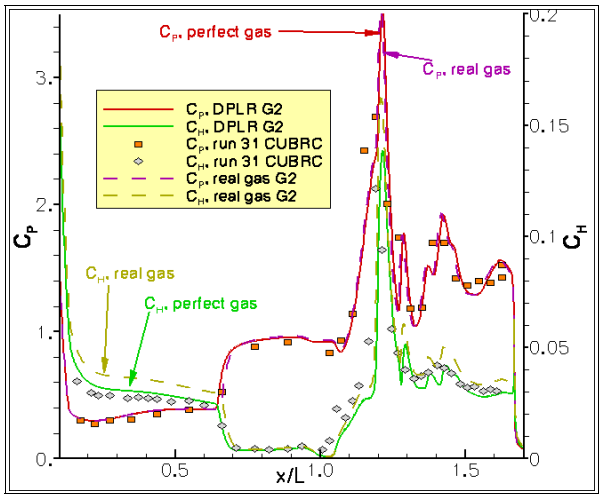

Figure 23. *Comparison of Blunt Nose Wall Data Results for Perfect Gas and Real Gas Models with DPLR Code*

Finally, the comparison between the perfect gas computations was assessed by comparing to the solution from the DPLR code with finite rate vibration and 2-species chemistry active. As shown in Fig. 23, the solutions are very similar. There is even less difference than was apparent in the sharp nose case. With the blunt nose case, like the hollow cylinder flare, only the leading cone heat transfer rates seem to be significantly impacted by the assumption of a perfect

gas model, along with the no slip wall boundary violation.

Although the separation region is not as enlarged as it was for the sharp case in Fig. 18, the change in separation point is much smaller here than it was for the sharp nose case. This points shifts by only about 0.01 *x/L* in this case. These two cases were actually solved using one of the initial exploration grids from the early investigation. Therefore, one can also see the consistency that the DPLR code provides on very different grids by comparing Fig. 22 and Fig. 23.

VALIDATION AND VERIFICATION

With the numerical results presented, some discussion must be made of verification, or numerical modeling errors. This issue has been discussed in a qualitative way in the previous sections in the form of the presentation of the surface pressure coefficient for each grid sequence. Here, some more quantitative results will be presented along with some general comments.

In most CFD studies, ordered discretization error tends to dominate the uncertainty in the solution. This is the error that tends to zero as the grid is refined to infinite density. Other major sources of error in this type of simulation include incomplete convergence error and boundary placement error. Fortunately, the characteristic propagation of hypersonic flows limits the zone of influence of a flow boundary. For example freestream boundary placement needs only to be outside of the region of travel of the bow shock from the models. For this reason, hypersonic boundaries are often quite simple, and standard boundary conditions were employed here.

Iterative convergence error will also be dealt with in a simple way. For DPLR, where the tight coupling of the viscous gradients into the implicit structure created a smooth, decreasing trend in residual levels, the solution for all grids and cases was iterated until approximately 7 to 8 orders of magnitude of residual reduction in continuity equation was obtained. The applicability of this level of convergence was verified by examining solutions of the surface pressure and heat transfer data for some of the grids to insure that the solution was no longer significantly changing.

For WIND, the magnitude of the residual dropped only nominally 3 orders of magnitude for numerical blocks that spanned the separated region. This was hypothesized to be a result of two possible causes – limit cycling resulting from the Min-Mod limiter, or (more likely) shock oscillation in the shock interaction region around the re-attachment point. Fortunately, WIND has a feature which allows monitoring of zonal loads, i.e. lift and drag. Although these forces are not directly of interest in the problem, monitoring of loads allows for an estimate of the stability of the shock positions in the solution. Problems were run until the oscillation magnitude of the forces was on the order of 0.1% of the nominal value or less as a criteria to determine convergence state.

Therefore, as is typical in this type of analysis, grid convergence error becomes the dominant source of numerical, or verification, error. Since this study was carefully prepared with several successive grids, an error analysis was made to assess the convergence rate of the codes. Although a detailed study of convergence behavior of these problems is a topic in itself, some cursory observations may be made.

To ascertain the effect of grid convergence error on each case, a representative quantity from the solution needs to be chosen. Here, in both the hollow cylinder flare and the double cone cases, the peak pressure level, the peak heating level, and the axial location of each peak has been chosen as important representative solution quantities.

The hollow cylinder case will be discussed first. From Roy[16], it is possible to perform a mixed-order analysis using the four available solutions from the grids G2 through G5 as defined by Table 2. Although WIND uses a 2ND order convective operator and DPLR used a 3RD order convective operator, Fig. 7 showed the convergence behavior of the two codes to be virtually identical, thus verifying Roy's indication that the observed order of convergence often has very little to do with the formal order of the scheme and is dominated by the presence of the shock interactions and necessary reconstruction limiter. The same type of analysis was performed for the sharp nose double cone and the blunt nose double cone cases using the grid sequence where the best available solutions on both codes were available.

With four solution levels, each with a refinement ratio of exactly 2.0, terms from the first, second, and third order may be evaluated, along with the error estimator E_1. An estimate of E_1 based similarly on 2 grid levels was given in Eqn. (3). As details of the equation development are not presented here, interested readers are referred to Appendix A of Ref. 16 for more information. In looking at the four degrees of freedom that have been selected for the hollow cylinder case – maximum C_P, maximum C_H, *x/L* location of maximum C_P, and *x/L* location of maximum C_H – it was found that the third order term is approximately zero in all four cases. Likewise, the degrees of freedom themselves were found to show a low level of second order dependency, meaning that both the maximum C_P and C_H are converging at approximately a first order rate with only a small amount of non-monotonicity. The axial location of those degrees of freedom, however, show first and second order terms of approximately equal strength, thus demonstrating a fully mixed-order convergence (somewhere between 1ST and 2ND order). This trend was true of all cases.

Finally, from this analysis, the error estimators for the degrees of freedom and their locations are presented in Table 3. Some care was exercised in calculating these values for the double cone cases because of the lack of steady-state convergence seen from the G1 grid with the WIND code. Thus, for both codes, the G2 through G5 sequences were first used in evaluating the grid dependency estimators so that the codes could be more directly contrasted. Additionally, the finer G1 through G4 sequence was used for the DPLR code to evaluate the same estimator. These values are also given in Table 3 as labeled.

First, one may see that the DPLR code performs slightly better in terms of ordered discretization error than the WIND code does fro a given sequence of grids. Comparison of the finer and coarser sets of values from the DPLR code shows that much improved error levels are seen by adding one further grid density step. Depending on the error levels required for an application, this extra grid level may be needed.

Table 3. *Grid Convergence Error Estimator, E_1, Magnitude Summary for Non-Monotonic Convergence Analysis over 4 Grid Levels*

case		$C_{P,MAX}$	x/L of C_P	$C_{H,MAX}$	x/L of C_H
Hollow Cylinder Flare		8.50%	0.76%	2.70%	3.40%
Sharp Nose Double Cone	DPLR G1	0.08%	0.08%	0.54%	0.11%
	DPLR G2	3.07%	1.00%	3.41%	1.39%
	WIND G2	16.20%	5.30%	35.10%	7.00%
Blunt Nose Double Cone (G2 Grid)	DPLR G1	0.01%	0.04%	0.61%	0.04%
	DPLR G2	2.63%	0.92%	4.91%	1.30%
	WIND G2	20.00%	8.57%	41.80%	9.30%

The relatively high values of numerical uncertainty for the pressure and heat transfer coefficients speak to the difficulty in computing solutions for these types of problems. The peak level and position was chosen because it is the most difficult aspect of the solution to predict with fidelity, and thus is presented as a worst-case scenario.

It is clear that the peak levels themselves in all cases are more uncertain than the position on the wall at which this peak level occurs. This is reflected in the higher observed order of convergence seen in the location parameters as discussed above. Also, Table 3 shows that the maximum pressure coefficient displays the highest level of error for the hollow cylinder while the heat transfer coefficient displays the highest level in both double cone cases.

QUALITATIVE OBSERVATIONS

Some general qualitative observations may also be made from this study besides the numerical results that have been discussed already. In terms of numerical construction, DPLR and WIND are very different codes and significant general insight may be obtained by looking at the behaviors of the algorithms used.

In general, the double cone cases were found to be more difficult than the hollow cylinder flare. This fact was particularly emphasized by the problems experienced with the WIND code when too fine a grid spacing was used in the separated region.

For both the sharp and the blunt nose double cone, initializing the solution proved to be difficult for both codes. Both codes initialize the flowfield to the freestream specification by default. For DPLR, it was necessary to start at an exceptionally low CFL for some number of iterations to relax into the solution before the effective timestep could be raised to a more practical level. Although this is often the case with this type of line relaxation algorithm, the double cone problems proved to be particularly delicate. For the WIND code, the CFL number also had to be reduced to 0.1 or lower and brought up very slowly. WIND also provides wall boundary relaxation during the starting process, an option which was left on. Even with these features active, the default second order Roe operator was found to be somewhat unstable during the initial start. The option "TEST 200 1", which prevents WIND from looking for negative speed of sound values calculated from the Roe scheme was also required. After a converged solution was obtained, there were no remaining negative values – this was necessary only during the first few iterations.

Because WIND employs local time stepping and DPLR employs global time stepping with several line relaxation sub-steps, making any direct comparisons between the convergence behavior is

difficult. However, it may be generally stated that the overall amount of computing time required to solve the problem satisfactorily on a given grid was approximately similar with both codes. DPLR, due to the fact that several line relaxation sub-steps are performed during a given iteration, was found to run much slower than WIND on a per iteration basis. However, it tended to converge in many fewer iterations than WIND, offsetting the deficit of decreased solution speed.

The most significant issue for the double cone cases was that of vibrational non-equilibrium modeling. Vibrational non-equilibrium is known to be a common issue in many hypersonic applications. Here, it was shown to play a role in determining the separation length in the sharp nose double cone case. Despite this limitation, the perfect gas model was shown to provide reasonable estimates for peak heating and pressure levels in the cases studied so far. The issue with regard to vibrational non-equilibrium, therefore, becomes an issue of what is to be considered important in obtaining a solution in a problem of this type.

CONCLUSIONS

In conclusion, it has been shown that both the WIND code from the NPARC Alliance and the DPLR code from NASA Ames Research Center are capable of capturing many of the effects seen in hypersonic shock-shock interaction problems like the hollow cylinder flare and the double cone geometries using a perfect gas N_2 model. In the majority of cases, the separation length was reasonably well predicted and peak levels of pressure and heating on the model surface were either accurately or conservatively predicted when a sufficiently fine grid was used.

The WIND code was shown to exhibit more sensitivity to the grid than DPLR, which converged consistently and independently of the grid spacing in the separated region. With proper grid construction, the WIND code was found to be capable of predicting the separation region length and peak levels. The low-dissipation scheme found in WIND seems to better represent the experimental data based on the constraints of a perfect gas, although this effect could not be studied in conjunction with non-equilibrium effects to assess the possibility of numerical error cancellation and the effect of the numerical scheme choice on those errors.

Although experimentation using N_2 as a test fluid removed the aspect of chemical reaction in the computation of the flowfield, the issue of vibrational non-equilibrium effects on the problems was shown to have some effect on the outcome for some cases. This was shown to affect the sharp nose double cone model case in particular, decreasing separation length by a significant percentage. Despite this effect, however, peak levels of heating and pressure were not strongly dependent on vibrational energy. The perfect gas model (independent of either code) was found to display a feature of offsetting errors contributed by insufficient grid resolution and neglect of freestream vibrational energy. A similar trend was seen with freestream vibrational energy and violation of the no-slip boundary condition with respect to heat transfer levels.

Further, it was shown that both codes, WIND and DPLR, displayed similar grid convergence behavior which was found to be of mixed order and observed to be below the formal order of accuracy of either code. This effect is attributed to order reduction through the shocks in the domain, which dominate the convergence behavior of the problem.

In general, on properly constructed grids at least, WIND and DPLR were shown to provide similar results using the perfect gas model despite the differences in numerical construction of the codes. This result helps to validate both codes as viable tools for these types of problems when sufficient care is taken to understand the limitations and included validation errors of the perfect gas model with regard to the issues discussed already.

ACKNOWLEDGEMENTS

- The WIND code provided by the NPARC Alliance and used under agreement.
- The DPLR code provided by NASA Ames Research Center and used under agreement.
- Special thanks to Dr. Michael Wright of NASA Ames for providing expertise and support in using DPLR to solve these problems.
- Special thanks to Dr. Graham Candler and Ioannis Nompelis of the University of Minnesota for their previous efforts in analyzing the double-cone flows and technical advice with this work.
- Some of the simulations in this work were supported in part by a grant of HPC computing time from the Arctic Region Supercomputing Center (ARSC).

REFERENCES

1. Holden, Michael S. and Wadhams, Timothy P. "A Database of Aerothermal Measurements in Hypersonic Flows in 'Building Block' Experiments for CFD Validation." AIAA 2003-1137. *41ST AIAA Aerospace Sciences Meeting & Exhibit*. Reno, NV. 6-9 January 2003.
2. Holden, M.S. and Parker, R.A. "LENS Hypervelocity Tunnels and Application to Vehicle Testing at Duplicated Flight Conditions." *Progress in Astronautics and Aeronautics: Advanced Hypersonic Test Facilities*. Vol 198. Frank K. Lu and Dan E. Marren, Ed. Chapter 4, Pages 73 – 110.

Reston, VA: American Institute of Aeronautics and Astronautics, 2002.
3. Olejniczak, Joseph; Wright, Michael J.; and Candler, Graham V. "Numerical Study of Inviscid Shock Interactions on Double-Wedge Geometries." Journal of Fluid Mechanics. Vol 352, Pages 1 – 25. 1997.
4. Candler, Graham V.; Nompelis, Ioannis; and Holden, Michael S. "Computational Analysis of Hypersonic Laminar Viscous-Inviscid Interactions." AIAA 2000-0532. 38TH AIAA Aerospace Sciences Meeting & Exhibit. Reno, NV. January 2000.
5. Holden, Michael S.; Wadhams, Timothy P.; Harvey, John K.; Candler, Graham V. "Comparisons between DSMC and Navier-Stokes Solutions on Measurements in Regions of Laminar Shock Wave Boundary Layer Interaction in Hypersonic Flows." AIAA 2002-0435. *40TH AIAA Aerospace Sciences Meeting & Exhibit*. Reno, NV. 14-17 January 2002.
6. Candler, Graham V.; Nompelis, Ioannis; Druguet, Marie-Claude; Holden, Michael; Wadhams, Timothy P.; Boyd, Iain D.; and Wang, Wen-Lan. "CFD Validation for Hypersonic Flight: Hypersonic Double-Cone Flow Simulations." AIAA 2002-0581. *40TH AIAA Aerospace Sciences Meeting & Exhibit*. Reno, NV. 14-17 January 2002.
7. NPARC WIND CFD Code, version 5, web site, <http://www.grc.nasa.gov/www/winddocs>. Accessed on 21 April 2003.
8. Wright, M.J.; Candler, G.V.; and Bose, D. "Data-Parallel Line Relaxation Method for the Navier-Stokes Equations." *AIAA Journal*. Vol 36, No 9, Pgs 1603 – 1609. September 1998.
9. Blottner, Frederick G. "Accurate Navier-Stokes Results for the Hypersonic Flow over a Spherical Nosetip." *AIAA Journal of Spacecraft and Rockets*. Vol 27, No 2, Pgs 113 – 122. March/April 1990.
10. American Institute of Aeronautics and Astronautics. *Guide for the Verification and Validation of Computational Fluid Dynamics Simulations*. AIAA G-077-1998. 1998.
11. Roache, Patrick J. *Verification and Validation in Computational Science and Engineering*. ISBN 0-913478-08-3. Albuquerque, NM: Hermosa Publishers, 1998.
12. Roy, C.J. "Grid Convergence Error Analysis for Mixed-Order Numerical Schemes." *AIAA Journal*. Vol 41, No 4, Pgs 595 – 604. April 2003.
13. Candler, Graham V.; Nompelis, Ioannis; Druguet, Marie-Claude. "Navier-Stokes Predictions of Hypersonic Double-Cone and Cylinder-Flare Flow Fields." AIAA 2001-1024. *39TH AIAA Aerospace Sciences Meeting & Exhibit*. Reno, NV. 8-11 January 2001.
14. Nompelis, I., Candler, G.V., and Holden, M.S. "effect of Vibrational Nonequilibrium on Hypersonic Double-Cone Experiments." AIAA Journal. Vol 41, No 11, Pgs 2162 – 2169. November 2003.
15. Anderson, John D. Jr. *Hypersonic and High Temperature Gas Dynamics*. ISBN 1-56347-459-X. Reston, VA: American Institute of Aeronautics and Astronautics, 2000. first printing McGraw-Hill, 1989.
16. Roy, Christopher J. "Grid Convergence Error Analysis for Mixed-Order Numerical Schemes." AIAA Paper 2001-2606. *15TH AIAA Computational Fluid Dynamics Conference*. Anaheim, CA. 11-14 June 2003.